Probing Electron Transfer Orbitals Selectively at $LiCoO_2$/C Cathode Interfaces via Positron Annihilation Spectroscopy

Meiying Zheng,[1,2,*] Jan Kuriplach,[3] Ilja Makkonen,[4] Rafael Ferragut,[1,2,5,†] Ekaterina Laakso,[2] Gioele Pagot,[6] Vito Di Noto,[6] and Bernardo Barbiellini[2,7,8,‡]

[1]*L-NESS and Department of Physics, Politecnico di Milano, Via Anzani 42, IT-22100, Como, Italy*
[2]*LUT School of Engineering Sciences, LUT University, Yliopistonkatu 34, FI-53850, Lappeenranta, Finland*
[3]*Department of Low Temperature Physics, Faculty of Mathematics and Physics, Charles University, V Holešovičkách 2, CZ-18000, Prague, Czech Republic*
[4]*Department of Physics, University of Helsinki, P.O. Box 43, FI-00014, Helsinki, Finland*
[5]*INFN Milano unit, National Institute for Nuclear Physics, IT-20133, Milano, Italy*
[6]*Section of Chemistry for the Technology (ChemTech) and INSTM, Department of Industrial Engineering, University of Padova, Via Marzolo 9, IT-35131, Padova, Italy*
[7]*Department of Physics, Northeastern University, Boston, Massachusetts 02115, USA*
[8]*Quantum Materials and Sensing Institute, Northeastern University, Burlington, Massachusetts 01803, USA*

(Received 20 October 2024; revised 9 May 2025; accepted 20 January 2026)

Conductive carbon additives in lithium-ion battery cathodes significantly increase electron transport, facilitating rapid charging. However, quantifying this improvement remains challenging. Momentum distribution of annihilating electron-positron pairs offers a powerful approach to selectively probe the O $2p$ orbitals in $LiCoO_2$ microparticles and the $2p_z$ carbon orbitals in the conductive carbon additives. By analyzing this momentum distribution, we obtain the amplification of subtle electron momentum distribution signals from carbon π bonds. *Ab initio* modeling of $LiCoO_2$ and various topologies of carbon structures reproducing the experimental momentum distribution helps to quantify the fraction of positron annihilation occurring within the carbon structures. Our theoretical results combined with earlier experimental findings reveal potential charge transport pathways in the $LiCoO_2$/C composite by quantifying the spectral contributions of electron transfer orbitals, which constitutes the nanoscale circuitry enabling efficient electron transport in battery cathodes.

DOI: 10.1103/9gfy-lxbp

Lithium-ion batteries (LIBs) are emerging as one of the most promising power sources for electric vehicles and portable smart devices. LIB cathodes typically feature a porous structure composed of micrograins of active materials—$LiCoO_2$ (LCO) in this case—along with a polymer binder, typically polyvinylidene difluoride (PVDF), and conductive carbon additives. Carbon coating is demonstrated to be benefit for cycle stability and rate capability [1,2]. The improvement in rate capability arises from enhanced electrochemical conductivity, including both ionic and electronic transport, which is essential for understanding the fast charging mechanism [3]. The boost of electron transport by carbon conductive network is well known, yet its quantum mechanical basis has not been fully explored. Because of the lack of reliable heterostructure models, accurately detecting electron transfer at buried interfaces relying solely on first-principles calculations remains significantly more challenging than their relative success in predicting ionic diffusion pathways [4–7]. Therefore, there is an urgent need for a reproducible feedback loop between theory, spectroscopy, and coating material design, capable of identifying and validating the mechanisms underlying fast charging mechanism.

In the carbon coated lithium cobalt oxide (LCO/C) cathode [8], the dominant electron transfer orbitals (ETO) at the interfaces include Co $3d$, O $2p$, and C $2p$ orbitals. As for the LCO active material, both Co $3d$ and O $2p$ orbitals contribute to reduction-oxidation (redox) processes. It is well known that transition-metal redox occurs in LCO [9], yet the contribution of oxygen to charge compensation has long been overlooked. In the past, only the Co $3d$ orbitals contribution was considered near the Fermi level in LCO, thereby underestimating ligand-to-metal electron sharing [10,11]. Moreover, projected density of states analyses based on muffin-tin radii partitioning downplay the oxygen

*Contact author: meiying.zheng@polimi.it
†Contact author: rafael.ferragut@polimi.it
‡Contact author: bernardo.barbiellini@lut.fi

contribution compared to Mulliken population analysis, as shown in Supplemental Material of Ref. [12]. Recent real space study [13] of the redox orbitals reveal high oxygen character across all Li concentrations. This result is also consistent with X-ray Compton scattering profile differences for various states of charge [12]. Theoretical analysis for LCO further support the interpretation of oxygen's role in charge transfer within mixed-valence systems [14,15], where Co $3d$ electrons strongly hybridize with O $2p$ orbitals, thereby enabling significant O $2p$ participation in the cathode redox reaction. This reaction can be written as $LiCoO_2 \leftrightarrow xLi^+ + Li_{1-x}CoO_2 + xe^-$, where Li^+ ions and electrons (e^-) are leaving the cathode upon battery charging.

Concerning the ETO in carbon, techniques such as X-ray absorption and emission spectroscopy can be employed to investigate the electronic structure of carbon. Experimental evidence from diamond, graphite, C_{70}, C_{60}, and benzene reveals distinct spectra influenced by π bands [16]. While X-ray techniques probe the band structure, they do not directly observe the actual motion of the electrons. Conversely, experiments measuring electron momentum density reveal how the momentum distribution of discrete orbitals evolves into conducting bands [17]. X-ray Compton scattering effectively elucidates electronic orbitals and proves particularly useful in identifying carbon p_z orbitals, which are crucial for conjugation in C—C and C═C bonds [18]. Interestingly, positrons, the antimatter counterparts of electrons, are very sensitive to the small electron momentum density signal originating from carbon's π bonding [19–24]. This property enables the detection of conductive pathways generated by the π band. By combining high-quality experimental data with modeling of electron-positron annihilating pairs, we can extract valuable information about O $2p$ redox orbitals in LCO and carbon $2p$ conducting orbitals, which are crucial for enhancing energy storage device performance [25].

Our previous calculations revealed significant charge redistribution from LCO to the C $2p$ orbitals after carbon coating, leading to a 1 eV downward shift of the Dirac point compared to pure graphite [7]. In this Letter, we analyze the ETO at LCO/C cathode interfaces using coincidence Doppler broadening (CDB) and two-component density functional theory (TCDFT), with details provided in the Appendix. CDB effectively characterizes positron annihilation sites within the composite cathode, comprising 93.75 wt% metal oxide particles, 4 wt% carbon structures, and 2.25 wt% of PVDF binder. The carbon ratio is an amount consistent with previous reports [5,26]. Positrons preferentially target the carbon π-bonding network [23] before annihilation, and we introduce the parameter β to quantify CDB contributions from carbon, revealing the electron transfer pathways. Thus, the positron serves as a selective quantum probe for studying ETO localized at the cathode interfaces.

Graphene, as a 2D π-conjugated material [27], can be either stacked into graphite [Fig. 1(a)], wrapped into fullerenes [Fig. 1(b)], or shaped into carbon nanotubes (CNTs) [Figs. 1(c) and 1(d)]. To characterize the spatial localization of electrons within these carbon polymorphs, we analyzed the electron localization function (ELF) [28–30]. This function takes values in the range between 0 and 1. As shown in Fig. 1, regions with high ELF values (ELF > 0.7) indicate localization of electrons in σ bonds, observable both in the flat sheets of graphite and the curved planes of C_{60} and CNTs. In contrast, an ELF value between 0.2 and 0.7 corresponds to delocalized behavior in the π-bonding network. And the ELF value $= 0$ to correspond to a delocalized system.

Figure 1 also shows the positron density distribution (PDD) $n_+(\mathbf{r}) = |\psi_+(\mathbf{r})|^2$ [31] for the graphite, C_{60}, CNTs, respectively. Our positron density calculations are based on the zero-density limit, involving a single positron per crystal [32]. In graphite, the main distribution of positron density confined between the graphene layers [see magenta regions in Fig. 1(a)], aligns well with our previous calculations [7]. In Fig. 1(b), the positron density results in C_{60} are presented on two planes, (001)-d_1 and (001)-d_2, defined by the distances, d_1 and d_2 from a reference plane perpendicular to the [001] direction to the bottom layer of C_{60}. $n_+(\mathbf{r})$ in the interstitial open volume [magenta regions in Fig. 1(b)] between the C_{60} molecules agrees well with the previous results [33–35]. For CNTs, we employ armchair CNTs [36], which are characterized by the chiral vector $\mathbf{C_h} = n_1\mathbf{a_1} + n_2\mathbf{a_2} \equiv (n_1, n_2)$, where n_1, n_2 are integers and $\mathbf{a_1}$, $\mathbf{a_2}$ are the primitive lattice vectors of graphene. In this configuration, the condition $n_1 - n_2 = 0$ classifies these CNTs as metallic, and their cylindrical structure is fully conjugated, supporting a delocalized π-electron system. In our Letter, we focus on chiral indices $(n_1, n_2) = (8, 8)$ and (12,12), referred to as CNT(8,8) and CNT(12,12), with diameters of 8.2 and 16.3 Å, respectively, are shown in Figs. 1(c) and 1(d). The latter's diameter is closer to that of the CNTs used in our experiments [8]. Results indicate that the positron wave function is confined in the interstitial region [magenta regions in Figs. 1(c) and 1(d)] of both CNT(8,8) and CNT(12,12) when employing our *ab initio* approach [37], agree with previous study [38]. From Fig. 1, we observe that positrons predominantly avoid regions with localized electrons in σ bonds, favoring regions where π bonds can form external to the carbon layers. Interestingly, several positron studies on carbon materials [19–24] confirm that positrons are attracted by π-electron regions. This attraction between the positron and π electron is particularly useful for detecting conduction networks. Notably, as natural electron acceptors, C_{60} and CNTs [39] can further promote positron attraction.

Regarding the electronic and positron states in LCO, our current TCDFT calculations using Vienna *ab initio*

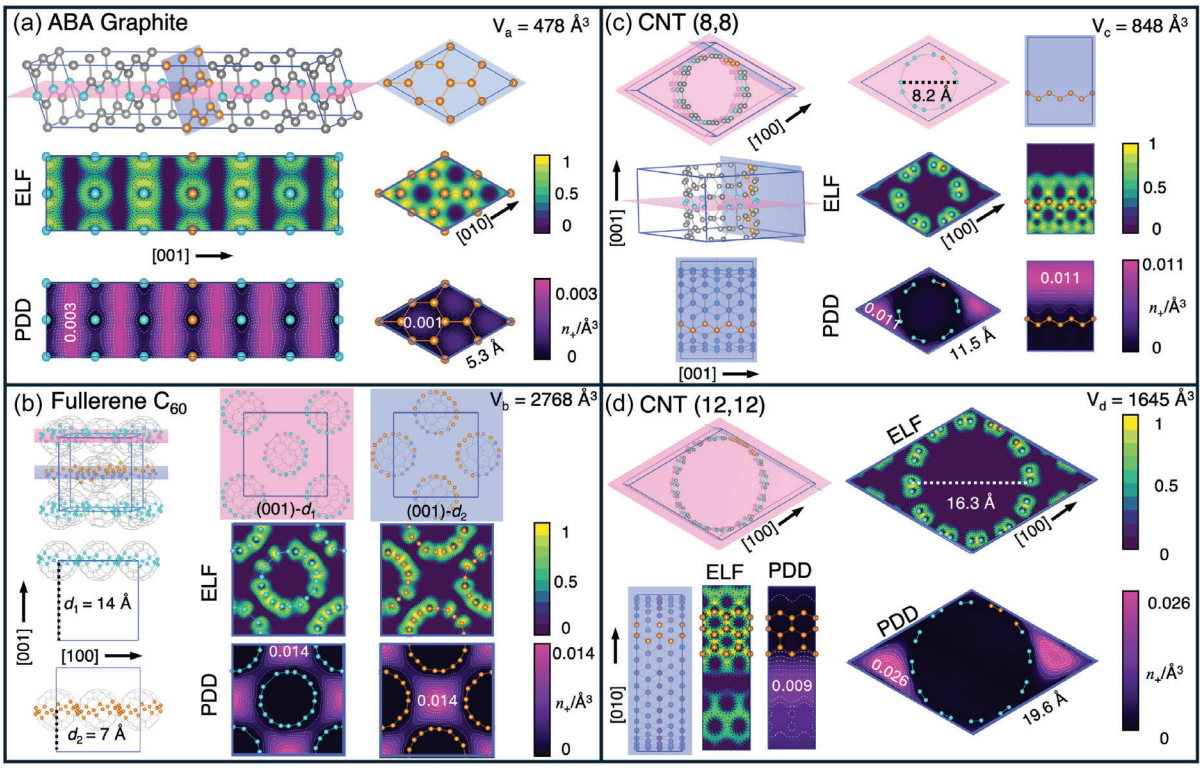

F1:1 FIG. 1. Calculations of the electron localization function (ELF) and positron density distribution (PDD) $n_+(\mathbf{r})$ in various carbon
F1:2 allotropes: (a) *ABA* graphite, (b) fullerene C_{60}, (c) carbon nanotubes CNT(8,8), and (d) CNT(12,12). We selected two distinct planes,
F1:3 represented by pink and blue, to display the results. Carbon atoms are denoted by cyan on the pink plane and by orange on the blue
F1:4 plane. Other carbon atoms are shown in gray. In C_{60}, the planes at different distances along the [001] direction are distinguished as
F1:5 (001)-d_1 and (001)-d_2. In CNTs, the blue plane reveals the bonding characteristics between conjugated carbon atoms, depicted as an
F1:6 orange chain. Density values reported herein are specific to each system and should not be directly compared, as they are influenced by
F1:7 the chosen packing density and normalization volume. Note the value of $n_+(\mathbf{r})$ depends on the periodic boundary conditions defined for
F1:8 the unit cells. The optimized six-layer *ABA* graphite was calculated with an in-plane lattice parameter of $a = 5.3$ Å and interlayer
F1:9 distance of 3.3 Å. C_{60} exhibits a cubic structure with a parameter $a = 14.0$ Å. In the case of carbon nanotubes, CNT(8,8) and CNT
F1:10 (12,12) possess diameters of 8.2 and 16.3 Å, respectively.

simulation package (VASP) [40] successfully reproduce previous results based on the electronic structure calculated with the WIEN2k method [31]. In particular, our present calculations confirm that the positron wave function has a strong overlap with the O $2p$ orbitals, which plays a key role in the redox reaction of the LCO cathode [12,14,15,41,42]. Knowledge of the electron and positron states allows us to calculate the momentum density of the annihilating electron-positron pairs [32,43]. From this, we can obtain the spherically averaged Doppler profile $I(p)$, which represents a one-dimensional projection of the electron momentum density since the positron momentum becomes negligible after thermalization. The contributions to $I(p)$ from the occupied orbital shells for LCO and carbon polymorphs are shown separately in Fig. 2. While the Li $2s$ orbital predominantly occupies the low momentum regions, the Co $3d$, O $2p$, and C $2p$ ETO exhibit significant contributions across both low and high momentum regions. This decay behavior is useful for fingerprinting different orbitals. Interestingly, the signal from the O $2p$ ETO in LCO [Fig. 2(a)] is strong due to the overlap with the positron wave function and the enhancement factor.

Next, we discuss the results of the Doppler profile for the ETO within carbon nanostructures. The positron overlap predominantly occurs with the p_z orbitals extending perpendicular to the sp^2-hybridized carbon atoms. These p_z orbitals contribute to π bonding, which is crucial for carbon conduction, and are thus characterized as conducting orbitals [27]. Although the carbon nanostructures show very similar Doppler profile [see Figs. 2(b)–2(d)], we highlight the differences by considering the ratios of the C $2p$ contribution to the total Doppler profile as shown in Fig. S1 of Supplemental Material [44]. The ratio curves for all carbon nanostructures show a prominent peak at 1.5 atomic units.

While for the carbon coated LCO heterostructures, our recent theoretical Doppler broadening calculations [45] modeled graphene stacked LCO with various terminations. In all cases, the major spectral contributions originate from

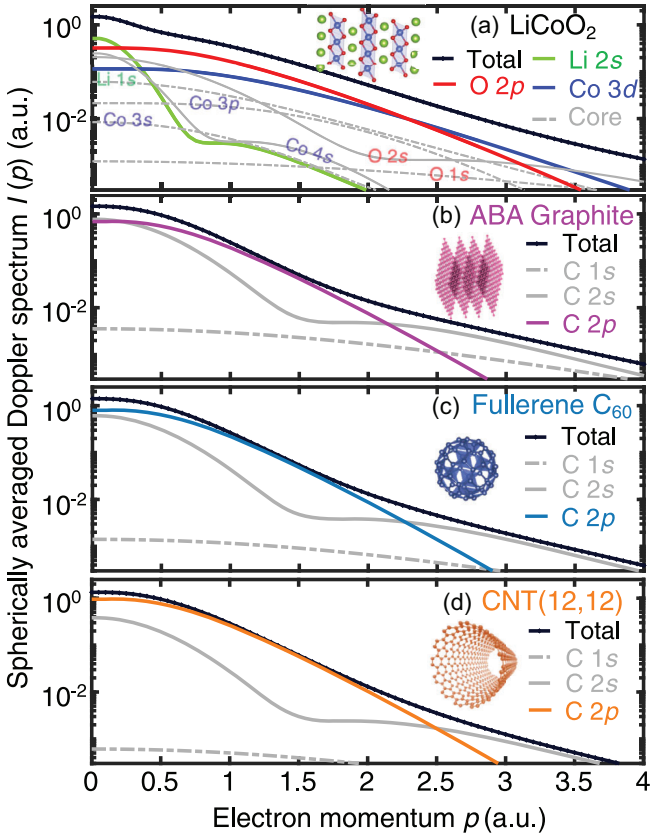

F2:1 FIG. 2. Calculated spherically averaged Doppler broadening
F2:2 spectrum $I(p)$ of the studied cathode material $LiCoO_2$ and carbon
F2:3 coating materials: (a) $LiCoO_2$, (b) *ABA* Graphite, (c) fullerene
F2:4 C_{60} and (d) CNT(12,12). Distribution of $I(p)$ as a function of the
F2:5 electron-positron annihilation pair's momentum p. Black lines
F2:6 indicate the total spectra, gray dashed lines indicate the core
F2:7 orbital contribution. Key valence orbitals are highlighted using
F2:8 color coding. Results show that positron, as a quantum probe, is
F2:9 particularly sensitive to valence orbitals, traversing in interstitial
F2:10 regions until trapping or annihilation.

C $2p$, O $2p$, and Co $3d$ ETO, illustrating that positron annihilation selectively highlights the momentum-space features of $2p$ orbitals, which are often less distinguishable in band and density of states analysis [5,7,46]. However, due to the computational limitation, constructing corresponding C_{60} or CNT-coated LCO heterostructure and quantifying the ETO contribution at the interfaces remain significant challenges for *ab initio* calculations thereby hindering high-throughput studies. Thus, to remove computational bottlenecks, we introduce a hybrid theoretical-experimental method based on a linear combination of LCO and carbon Doppler profile contributions to derive the β parameter accurately. Therefore, we introduce a linear combination method based on the Doppler profiles obtained from TCDFT simulations of various carbon-coated structures and LCO.

First, starting from the spherically averaged Doppler profile $I(p)$, we calculate the directional average of the momentum distribution $N(p)$ given by [47]

$$N(p) = -\frac{\mathrm{d}I(p)}{\mathrm{d}p}p. \tag{1}$$

Then we use TCDFT results to model a linear combination of LCO and carbon samples for comparison with experimental carbon coated LCO:

$$N(p) = (1-\beta)\,N(p)_{\mathrm{LCO}} + \beta\,N(p)_{\mathrm{C}}, \tag{2}$$

where β is the fraction of positron annihilation within carbon structures, $N(p)_{\mathrm{LCO}}$ and $N(p)_{\mathrm{C}}$ are the momentum distribution of LCO and various carbon samples, respectively. The TCDFT calculated $N(p)$ results for LCO, graphite, C_{60}, CNTs and linear fitting curves are shown in Fig. 3. The corresponding experimental data shown in this figure is taken from our previous work [8]. The momentum density peak of graphite at 0.9 a.u. is consistent with previous research [47]. A shift from O $2p$ to C $2p$ ETO in all cases is observed, aligning well with the experimental results [8]. Table I gives the results of the linear combination in Eq. (2) for the LCO cathode and various carbon morphologies.

Our previous broadband electrical spectroscopy (BES) studies [8] have quantitatively demonstrated that even a mere 4 wt% addition of carbon can significantly increase the Li-ion mobility and electron conductivity of LCO cathodes by 2 orders of magnitude, depending on the type of carbon—super P (SP), nanosphere (XC), and nanotubes (NT). The electrochemical performance at moderate high C rates confirmed this, following the trend NT > XC > SP, while the carbon-free electrode (NoC) performs worst. Li-ion diffusion coefficients extracted from BES, plotted as a function of the carbon additive (see Fig. S2(a) in Supplemental Material [44]). Furthermore, our recent positron annihilation lifetime spectroscopy results [7,8] indicate two lifetime components observed in all carbon coated LCO samples, the first lifetime component attributed to LCO bulk, while the second lifetime leading to the positron surface states associated to LCO/C interface. Interestingly, the intensity of the second lifetime I_2 increased by following the trend consistent with BES results, as shown in Figs. S2(a) and S2(b) of Supplemental Material [44]. For pristine LCO, the implanted positrons are not expected to reach the grain boundaries within the cathode [8], and theoretically, we anticipate a β value close to 0. Actually, the LCO sample used in our previous experiment—referred to as NoC—is composed of 2.25 wt% PVDF $[(CH_2\text{-}CF_2)_n]$ and 97.75 wt % LCO. As a result, the linear fitting of the NoC experimental data yields a β value of 0.15. This discrepancy consistently appears and is compliant with the density functional theory (DFT)-calculated heterostructure results [45], as highlighted in the cyan region of Fig. S2(c) in Supplemental Material [44]. And Fig. S3 [44] compares the

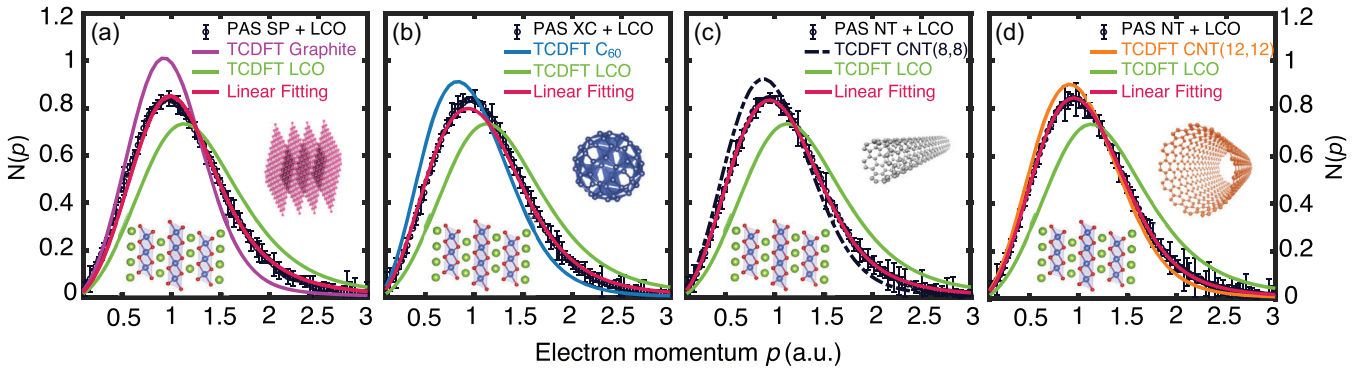

F3:1 FIG. 3. Momentum distribution, $N(p)$ for calculated LCO and carbon, along with their linear combination, compared with
F3:2 experimental results from diverse samples. The PAS experimental momentum profiles for different samples in (a) super P—SP,
F3:3 (b) carbon nanospheres—XC, and (c),(d) carbon nanotubes—NT, are represented by black lines. The TCDFT calculated momentum
F3:4 distributions for LCO, graphite, C_{60}, CNT(8,8), and CNT(12,12) are color coded by green, magenta, blue, black (dashed), and orange
F3:5 lines, respectively. The theoretical linear combinations of the calculated spectra, as denoted by Eq. (2), are shown in red lines. These
F3:6 profiles are instrumental in identifying the high-momentum electron contributions, serving as a chemical fingerprint of the annihilation
F3:7 sites. The experimental data are derived from our previous work [8]. The distribution $N(p)$ is normalized to one.

PAS-measured and DFT-calculated momentum densities for NoC, with PAS statistical uncertainties indicated by error band.

It should be noted that all carbon-mixed LCO cathodes maintain a consistent weight composition ratio of 2.25:4.00:93.75 for PVDF, C, and LCO, respectively. The variable among these samples [super P (SP), carbon nanospheres (XC), and carbon nanotubes (NT)] is their morphology [8]. Surprisingly, in all cases of LCO + carbon, the fitting β value ranges from 0.48 to 0.74, in spite of only 4 wt% carbon, agrees well with the experimental [8] and theoretical [45] results. The increase in β is attributed to the attraction of the positron to the π bonds, reflecting higher free electron density in the π band and improved conductivity. As a matter of fact, fullerenes and CNTs, as natural electron acceptors, show higher β values compared to the graphite. Molecular orbital theory explains how CNTs can be semiconducting or metallic, with low-lying π^* orbitals that readily accept electrons, boosting electron transport along the tube axis. This phenomenon, initially shown in C_{60}, extends to tubular carbon structures [39]. Thus, these results establish β as a key descriptor to detect electrically conductive pathways.

In conclusion, our Letter demonstrates the potential of positron selectivity in distinguishing between different atomic orbitals, providing valuable insights into electron transfer orbitals within buried interface in cathode materials. Therefore, it could be useful to study advanced interfacial conduction theory at solid-liquid battery interfaces [48]. The amplified CDB signals, characterized by the β parameter, specifically reveal the contribution of $2p_z$ carbon orbitals associated to efficient electron transport, particularly in carbon nanotubes. Our positron annihilation analysis of various carbon morphologies in LCO-based cathodes opens up new possibilities for exploring topological carbon physics discussed by Chen *et al.* [27]. This approach not only deepens our understanding of fast charge mechanism based on electron transport, but also aids in screening coating materials for next-generation battery technologies. Our Letter motivates future studies to incorporate morphological models of carbon-coated heterostructures to directly identify and quantify electron transfer orbitals, including those in hybrid and disordered carbon systems.

TABLE I. The β parameter extracted for various carbon coating structures: positron annihilation spectroscopy (PAS) measurements (β_0) [8], DFT calculations (β_1) [45], and linear combination fitting (β). The experimental samples of NoC refers to LCO without carbon coating, while SP, XC, NT correspond to LCO coated with super P, carbon nanospheres, and carbon nanotubes, respectively. The DFT LCO/C refers to graphene layers stacked LCO heterostructures.

PAS [8]	β_0	DFT [45]	β_1	Linear combination	Fitted β	Adjusted R^2 (%)
NoC	···	LCO	0	LCO	0.15	99.135
SP	0.45(3)	LCO/C	0.29–0.34	LCO + Graphite	0.48	99.712
XC	0.55(4)	LCO/C_{60}	···	LCO + C_{60}	0.58	99.743
NT	0.60(3)	LCO/CNT	···	LCO + CNT(8, 8)	0.64	99.976
				LCO + CNT(12, 12)	0.74	99.978

Acknowledgments—M. Z. gratefully acknowledges a grant from the China Scholarship Council and a research fund from Politecnico di Milano (Polimi). This research was also supported by the Ministry of Education and Culture (Finland), Polimi (Italy), and the LUT INERCOM Platform. The authors acknowledge the CSC —IT Center for Science, Finland for computer time and the ELMO-LION doctoral summer school funded by EIT Raw Materials for educational resources. J. K. acknowledges the support from the Ministry of Education, Youth and Sports of the Czech Republic through the e-INFRA CZ (ID: 90254). G. P. and V. D. N. thank (1) the program "Budget Integrato per la Ricerca Interdipartimentale–BIRD 2021" of the University of Padova (project ACHILLES, protocol number BIRD219831); (2) the Italian National Recovery and Resilience Plan (NRRP), Mission 04 Component 2, Investment 1.5–NextGenerationEU, PE2 NEST–Network 4 Energy Sustainable Transition, Spoke 6 Energy Storage; and (3) the project "ORgANics for Green Electrochemical Energy Storage Project (ORANGEES)" funded by MASE "PT 2019-2021, DD 27.10.2021 bando a, DD 05.08.2022."

Data availability—The data that support the findings of this article are openly available [49].

[1] M. Chaudhary, S. Tyagi, R. K. Gupta, B. P. Singh, and R. Singhal, Surf. Coat. Technol. **412**, 127009 (2021).
[2] J. F. Baumgärtner, K. V. Kravchyk, and M. V. Kovalenko, Adv. Energy Mater. **15**, 2400499 (2025).
[3] C. Zhu, R. E. Usiskin, Y. Yu, and J. Maier, Science **358**, eaao2808 (2017).
[4] M. Park, X. Zhang, M. Chung, G. B. Less, and A. M. Sastry, J. Power Sources **195**, 7904 (2010).
[5] J. Lin, C. Zeng, Y. Chen, X. Lin, C. Xu, and C.-Y. Su, J. Mater. Chem. A **8**, 6607 (2020).
[6] J. Lin, Y.-H. Sun, and X. Lin, Nano Energy **91**, 106655 (2022).
[7] M. Zheng, J. Kuriplach, I. Makkonen, R. Ferragut, V. Di Noto, G. Pagot, E. Laakso, and B. Barbiellini, Commun. Mater. **5**, 138 (2024).
[8] G. Pagot, V. Di Noto, K. Vezzù, B. Barbiellini, V. Toso, A. Caruso, M. Zheng, X. Li, and R. Ferragut, Iscience **26**, 105794 (2023).
[9] M. D. Johannes, C. T. Love, and K. Swider-Lyons, in *Springer Handbook of Electrochemical Energy* (Springer, New York, 2016), pp. 313–328.
[10] J. Yin, Z. Wu, K. Fang, Y. Zhu, K. Zhang, H. Zhang, Y. Chen, L. Li, L. Fan, K. Dong *et al.*, Chem. Sci. **16**, 8268 (2025).
[11] M. J. Ogley, A. S. Menon, G. C. Pandey, G. J. P. Fajardo, B. J. Johnston, I. McClelland, V. Majherova, S. Huband, D. Tripathy, I. Temprano *et al.*, Joule **9**, 101775 (2025).
[12] B. Barbiellini, K. Suzuki, Y. Orikasa, S. Kaprzyk, M. Itou, K. Yamamoto, Y. J. Wang, H. Hafiz, R. Yamada, Y. Uchimoto *et al.*, Appl. Phys. Lett. **109**, 073102 (2016).
[13] T. Shang, D. Xiao, F. Meng, X. Rong, A. Gao, T. Lin, Z. Tang, X. Liu, X. Li, Q. Zhang *et al.*, Nat. Commun. **13**, 5810 (2022).
[14] T. Mizokawa, Y. Wakisaka, T. Sudayama, C. Iwai, K. Miyoshi, J. Takeuchi, H. Wadati, D. Hawthorn, T. Regier, and G. Sawatzky, Phys. Rev. Lett. **111**, 056404 (2013).
[15] R. Fantin, A. van Roekeghem, and A. Benayad, PRX Energy **2**, 043010 (2023).
[16] J. Guo, J. Phys. Chem. Solids **69**, 2223 (2008).
[17] M. Vos and I. McCarthy, Rev. Mod. Phys. **67**, 713 (1995).
[18] P. Eisenberger and W. Marra, Phys. Rev. Lett. **27**, 1413 (1971).
[19] E. Arthur-Baidoo, J. Danielson, C. Surko, J. Cassidy, S. Gregg, J. Hofierka, B. Cunningham, C. Patterson, and D. Green, Phys. Rev. A **109**, 062801 (2024).
[20] J. R. Danielson, S. Ghosh, and C. M. Surko, Phys. Rev. A **106**, 032811 (2022).
[21] Y. Sugiura, T. Takayanagi, Y. Kita, and M. Tachikawa, Eur. Phys. J. D **73**, 1 (2019).
[22] N. Djourelov, T. Suzuki, R. Yu, and Y. Ito, Nucl. Instrum. Methods Phys. Res., Sect. A **540**, 487 (2005).
[23] S. Berko, R. Kelley, and J. Plaskett, Phys. Rev. **106**, 824 (1957).
[24] M. Hasegawa, M. Kajino, H. Kuwahara, E. Kuramoto, M. Takenaka, and S. Yamaguchi, Mater. Sci. Forum, **105**, 1041 (1992).
[25] J. Nokelainen, B. Barbiellini, J. Kuriplach, S. Eijt, R. Ferragut, X. Li, V. Kothalawala, K. Suzuki, H. Sakurai, H. Hafiz *et al.*, Condens. Matter **7**, 47 (2022).
[26] X. Qi, B. Blizanac, A. DuPasquier, M. Oljaca, J. Li, and M. Winter, Carbon **64**, 334 (2013).
[27] Y. Chen, Y. Xie, X. Yan, M. L. Cohen, and S. Zhang, Phys. Rep. **868**, 1 (2020).
[28] A. D. Becke and K. E. Edgecombe, J. Chem. Phys. **92**, 5397 (1990).
[29] A. Savin, O. Jepsen, J. Flad, O. K. Andersen, H. Preuss, and H. G. von Schnering, Angew. Chem., Int. Ed. Engl. **31**, 187 (1992).
[30] E. Matito and M. Solà, Coord. Chem. Rev. **253**, 647 (2009).
[31] B. Barbiellini and J. Kuriplach, J. Phys. Conf. Ser. **791**, 012016 (2017).
[32] F. Tuomisto and I. Makkonen, Rev. Mod. Phys. **85**, 1583 (2013).
[33] M. Puska and R. Nieminen, J. Phys. Condens. Matter **4**, L149 (1992).
[34] S. Ishibashi and M. Kohyama, Phys. Rev. B **67**, 113403 (2003).
[35] Y. Ito and T. Suzuki, Phys. Rev. B **60**, 15636 (1999).
[36] R. Saito, M. Fujita, G. Dresselhaus, and M. Dresselhaus, Appl. Phys. Lett. **60**, 2204 (1992).
[37] B. Barbiellini, M. J. Puska, T. Torsti, and R. M. Nieminen, Phys. Rev. B **51**, 7341 (1995).
[38] S. Ishibashi, J. Phys. Condens. Matter **14**, 9753 (2002).
[39] D. M. Guldi, G. Rahman, F. Zerbetto, and M. Prato, Acc. Chem. Res. **38**, 871 (2005).
[40] G. Kresse and J. Furthmüller, Phys. Rev. B **54**, 11169 (1996).
[41] D. Asakura, T. Sudayama, Y. Nanba, E. Hosono, H. Kiuchi, K. Yamazoe, J. Miyawaki, Y. Harada, A. Yamada, R.-P. Wang *et al.*, Phys. Chem. Chem. Phys. **27**, 4092 (2025).
[42] U. Patel, T. Guruswamy, A. Krzysko, H. Charalambous, L. Gades, K. Wiaderek, O. Quaranta, Y. Ren, A. Yakovenko, U. Ruett *et al.*, Rev. Sci. Instrum. **93**, 11310 (2022).

[43] S. W. Eijt, A. Van Veen, H. Schut, P. E. Mijnarends, A. B. Denison, B. Barbiellini, and A. Bansil, Nat. Mater. **5**, 23 (2006).
[44] See Supplemental Material at http://link.aps.org/supplemental/10.1103/9gfy-lxbp for (Fig. S1) Doppler profile ratio of C $2p$ orbital contributions across various carbon materials; (Fig. S2) Functional role of carbon coatings in $LiCoO_2$/C cathodes; and (Fig. S3) Comparison between experimental and calculated momentum density for uncoated LCO, which includes Refs. [8,45].
[45] M. Zheng, I. Makkonen, R. Ferragut, J. Kuriplach, E. Laakso, V. Di Noto, G. Pagot, and B. Barbiellini, Electrochim. Acta **526**, 146128 (2025).
[46] S. Gong, S. Wang, J. Liu, Y. Guo, and Q. Wang, J. Mater. Chem. A **6**, 12630 (2018).
[47] A. Stewart, Can. J. Phys. **35**, 168 (1957).
[48] J. Halldin Stenlid, P. Zguns, D. Vivona, A. Aggarwal, K. Gordiz, Y. Zhang, S. Pathak, M. Z. Bazant, Y. Shao-Horn, Baskin *et al.*, ACS Energy Lett. **9**, 3608 (2024).
[49] M. Zheng, R. O. Ferragut, and B. Barbiellini, Dataset: Probing Electron Transfer Orbitals Selectively at LiCoO2/C Cathode Interfaces via Positron Annihilation Spectroscopy, Version v1, Zenodo (2026), 10.5281/zenodo.18764935.
[50] M. Alatalo, B. Barbiellini, M. Hakala, H. Kauppinen, T. Korhonen, M. J. Puska, K. Saarinen, P. Hautojärvi, and R. M. Nieminen, Phys. Rev. B **54**, 2397 (1996).
[51] A. Calloni, A. Dupasquier, R. Ferragut, P. Folegati, M. Iglesias, I. Makkonen, and M. J. Puska, Phys. Rev. B **72**, 054112 (2005).
[52] G. Barucca, R. Ferragut, D. Lussana, P. Mengucci, F. Moia, and G. Riontino, Acta Mater. **57**, 4416 (2009).
[53] G. Riontino, D. Lussana, M. Massazza, G. Barucca, P. Mengucci, and R. Ferragut, J. Alloys Compd. **463**, 200 (2008).
[54] G. Panzarasa, S. Aghion, G. Soliveri, G. Consolati, and R. Ferragut, Nanotechnology **27**, 02LT03 (2015).
[55] P. Asoka-Kumar, M. Alatalo, V. J. Ghosh, A. C. Kruseman, B. Nielsen, and K. G. Lynn, Phys. Rev. Lett. **77**, 2097 (1996).
[56] P. E. Blöchl, Phys. Rev. B **50**, 17953 (1994).
[57] J. P. Perdew, A. Ruzsinszky, G. I. Csonka, O. A. Vydrov, G. E. Scuseria, L. A. Constantin, X. Zhou, and K. Burke, Phys. Rev. Lett. **100**, 136406 (2008).
[58] A. Jain, G. Hautier, S. P. Ong, C. J. Moore, C. C. Fischer, K. A. Persson, and G. Ceder, Phys. Rev. B **84**, 045115 (2011).
[59] L. Wang, T. Maxisch, and G. Ceder, Phys. Rev. B **73**, 195107 (2006).
[60] D. Bende, F. R. Wagner, O. Sichevych, and Y. Grin, Angew. Chem. **129**, 1333 (2017).
[61] S. Laubach, S. Laubach, P. C. Schmidt, D. Ensling, S. Schmid, W. Jaegermann, A. Thißen, K. Nikolowski, and H. Ehrenberg, Phys. Chem. Chem. Phys. **11**, 3278 (2009).
[62] E. Boroński and R. M. Nieminen, Phys. Rev. B **34**, 3820 (1986).
[63] M. J. Puska and R. M. Nieminen, Rev. Mod. Phys. **66**, 841 (1994).
[64] K. A. Simula, J. Härkönen, I. Zhelezova, N. D. Drummond, F. Tuomisto, and I. Makkonen, Phys. Rev. B **108**, 045201 (2023).
[65] K. A. Simula, J. E. Muff, I. Makkonen, and N. D. Drummond, Phys. Rev. Lett. **129**, 166403 (2022).
[66] J. Hofierka, B. Cunningham, C. M. Rawlins, C. H. Patterson, and D. G. Green, Nature (London) **606**, 688 (2022).
[67] B. Barbiellini and J. Kuriplach, Phys. Rev. Lett. **114**, 147401 (2015).
[68] D. Koelling and B. Harmon, J. Phys. C **10**, 3107 (1977).
[69] I. Makkonen, M. Hakala, and M. J. Puska, Phys. Rev. B **73**, 035103 (2006).
[70] A. C. L. Jones, H. J. Rutbeck-Goldman, T. H. Hisakado, A. M. Piñeiro, H. W. K. Tom, A. P. Mills Jr, B. Barbiellini, and J. Kuriplach, Phys. Rev. Lett. **117**, 216402 (2016).

End Matter

Appendix—The coincidence Doppler broadening (CDB) technique, which uses dual γ-ray spectrometers to detect two coincident photons originating from electron-positron annihilation, has demonstrated success in applications across semiconductors and metals [50–55]. Measured CDB profiles replicate the momentum distribution of annihilating electron-positron pairs, and reflect thus the local electronic chemical environments encountered by positron. The chemical fingerprints derived from such momentum densities offer invaluable insights into the studied material's properties.

We employed the Vienna *ab initio* simulation package (VASP) [40] to calculate the ground state properties of bulk systems. The projector augmented wave (PAW) method [56] and the Perdew-Burke-Ernzerhof (PBE) electron-electron exchange and correlation functional [57] were utilized during the relaxation processes. To account for the Coulombic interactions in the $3d$ electron shell of cobalt ions, we applied the generalized gradient approximation with an on-site Hubbard correction (GGA + U) [58], incorporating a Hubbard-type U term ($U - J = 3.3$ eV)[59]. A plane-wave cutoff energy of 400 eV effectively ensured convergence and we utilized a Γ-centered $9 \times 9 \times 1$ **k** mesh [60] for LCO with Gaussian smearing set at 0.2 eV. The optimized LCO hexagonal a and c parameter values were calculated to be 2.81 and 13.91 Å, respectively, consistent with the experimental lattice parameters [60]. A **k**-point spacing of $2\pi \times 0.04$ Å^{-1} was employed to generate Γ-centered **k**-point grids for sampling the carbon Brillouin zone. The convergence criterion was 1 0^{-4} eV for total energy. The core spectrum is a sum of the core orbital contributions (C $1s$, Li $1s$, Co $1s2s2p3s3d$, O $1s$), and the valence electrons were treated as the C $2s2p$, Li $2s$, Co $3d4s$, O $2s2p$ electrons.

To model the positron annihilation characteristics of delocalized positrons, two-component density functional theory (TCDFT) [62,63], in its zero positron density limit, was employed to calculate the momentum density of annihilating electron-positron pairs. TCDFT offers a favorable balance between the accuracy of many-body theories,

such as quantum Monte Carlo [64,65] and many-body perturbation theory [66], and computational efficiency. TCDFT relies on several approximations, including the electron-electron exchange-correlation functional, the electron-positron correlation functional, and momentum density models with enhancement factors [32]. These functionals are parametrized based on data from accurate many-body calculations. However, as DFT is fundamentally distinct from many-body perturbation theory, it is challenging to directly compare their accuracies or quantify the inclusion of virtual positronium formation within the DFT framework.

A parameter-free [67] GGA was applied to the electron-positron correlation potential and enhancement factor to capture the response of the electron gas to the positron. The calculated Doppler spectra were obtained by using the state-dependent model [50]. To enable Doppler profile decomposition in Figs. 2 and 3, we used the self-consistent potential and calculated the Doppler broadening using atomic orbitals, assuming a spherical symmetry of the positron wave function around nuclei. The core orbitals are determined by solving the Dirac equation, following the approach proposed by Koelling *et al.* [68]. In Fig. 2, we used reconstructed PAW orbitals for valence electrons [68] and calculated the spherical average of the Doppler spectrum using stochastic integration, which is appropriate when comparing with measurements of samples with randomly oriented grains. Before comparing with experimental data in Fig. 2, the theoretical spectra were convoluted with the experimental resolution function.

TCDFT's predictions for Doppler broadening and annihilation characteristics have been validated through comparison with experimental data and variational quantum Monte Carlo (VMC) method. Recent studies [64,65] have shown reasonable agreement between DFT models, experimental results, and VMC benchmarks for bulk materials. Furthermore, DFT's accuracy has been benchmarked in terms of positron and positronium affinities, achieving a precision of approximately 50 meV in solid-state systems like bulk copper [70]. While perturbative approaches, such as those based on Hartree-Fock ground states and self-energy corrections from virtual positronium diagrams [66], offer greater formal rigor, their application to complex systems like solids and interfaces remains computationally prohibitive. Consequently, DFT represents the most practical and feasible approach for studying these systems at present. Q1